Seasonal phasing of Agulhas Current transport tied to a baroclinic adjustment of near-field winds

Katherine Hutchinson[1,2], Lisa M. Beal[3], Pierrick Penven[4], Isabelle Ansorge[1] and Juliet Hermes[1,2]

[1]Department of Oceanography, University of Cape Town, Cape Town, South Africa.
[2]South African Environmental Observations Network, SAEON Egagasini Node, Cape Town, South Africa.
[3]Rosenstiel School of Marine and Atmospheric Science, University of Miami, Miami, FL, USA
[4]Laboratoire d'Oceanographie Physique et Spatiale, Univ. Brest, CNRS, IRD, Ifremer, IUEM, Brest, France.

Key Points:

- A baroclinic adjustment to Indian Ocean winds can explain the Agulhas Current seasonal phasing and a barotropic adjustment cannot.
- Seasonal phasing is found to be highly sensitive to reduced gravity values which modify adjustment times to wind forcing.
- Near-field winds have a dominant influence on the seasonal cycle of the Agulhas Current as remote signals die out while crossing the basin.

Corresponding author: Katherine Hutchinson, `kath.hutchinson@gmail.com`

Abstract

The Agulhas Current plays a significant role in both local and global ocean circulation and climate regulation, yet the mechanisms that determine the seasonal cycle of the current remain unclear, with discrepancies between ocean models and observations. Observations from moorings across the current and a 22 year proxy of Agulhas Current volume transport reveal that the current is over 25% stronger in austral summer than in winter. We hypothesize that winds over the Southern Indian Ocean play a critical role in determining this seasonal phasing through barotropic and first baroclinic mode adjustments and communication to the western boundary via Rossby waves. Our hypothesis is explored using single layer and one-and-a-half layer models. We find that the barotropic contribution to seasonal phasing is small, with the majority of the seasonal signal deflected offshore and along the Mozambique Ridge. The summertime maximum and wintertime minimum can, however, be reproduced by a one-and-a-half layer reduced gravity model in which adjustment time to wind forcing via Rossby waves is in line with observations from satellite altimetry. Additionally, near-field winds (to the west of 35°E) are shown to have a controlling influence on the seasonal phasing, as signals from farther afield dissipate through destructive interference with overlying winds before reaching the western boundary. These results suggest a critical role for a baroclinic adjustment to near-field winds in setting the summertime maximum in Agulhas Current transport.

1 Introduction

The Agulhas Current (AC) is the western boundary current of the South Indian Ocean subtropical gyre, hereafter referred to as the Southern Indian Ocean (Figure 1). The AC carries water poleward along the east coast of southern Africa and is the strongest western boundary current globally at 30° latitude [Bryden et al., 2005]. At the southern tip of Africa, the AC exports warm, saline Indian Ocean water into the South Atlantic via a process of ring shedding and filamentation. The current is consequently regarded as an essential limb of the Global Thermohaline Circulation [Beal et al., 2011]. At a regional scale the current exerts an influence on rainfall and climate over southern Africa [Njouodo et al., 2018]. Despite the important role of the AC in both ocean circulation and in moderating local and global climate, the principal processes that govern the seasonality in volume transport of the current are poorly understood.

Due to the historic deficiency of *in-situ* time-series data on the AC, studies focusing on the variability of this current have largely relied on ocean models or satellite data. Previous studies used ocean general circulation models (OGCMs) to predict an austral winter-spring maximum in transport of the AC [Biastoch et al., 1999; Matano et al., 2002]. Biastoch et al. [1999] used the 1/3° Modular Oceans Model (MOM2) and proposed that the spring (November) maximum in AC transport (blue line Figure 2) was advected from the Mozambique Channel. Matano et al. [2002] used the 1/4° Parallel Ocean Circulation Model (POCM) and suggested that the seasonality is controlled by barotropic modes that are forced directly by the winds, resulting in a winter (August) maximum in the current (red line Figure 2). Both these models are B-grid, z level, primitive equation, large scale circulation models derived from the Bryan-Cox-Semtner code. To the best of the authors' knowledge, no more recent model results on AC seasonality have been published. Krug and Tournadre [2012] used satellite altimetry and suggested the opposite seasonality, finding that the surface geostrophic currents are stronger in austral summer. There has been no direct work linking AC seasonality to the East Madagascar Current (EMC). While there is evidence for an upstream control of AC leakage linked to the EMC via the triggering of meanders [Schouten et al., 2000; Penven et al., 2006; Elipot and Beal, 2015], the EMC is not considered to be of primary importance in influencing AC seasonality as the south-westward transport of the AC was shown to be largely unaffected by the passing of a meander [Leber and Beal, 2104], and there is no evidence for seasonality in volume transport of the EMC [Nauw et al., 2008; Ponsoni et al., 2016].

An extensive set of *in-situ* measurements of the AC was recently obtained as part of the Agulhas Current Time-series (ACT) experiment. These measurements span the period from April 2010 to February 2013, providing 34 months of continuous velocity and transport data [Beal et al., 2015]. The 300 km long array left the South African coastline at 33.4°S following the path of a satellite altimeter groundtrack (Figure 1). Both the ACT mooring data, and a derived 22-year altimeter proxy for transport show that the current is strongest in austral summer (January-February-March), with a 25% increase in volume transport from the winter minimum (July-August) [Beal et al., 2015; Beal and Elipot, 2016]. Figure 2 shows the seasonal cycle of the proxy for the time period for which QuikSCAT was in operation (1999-2009). The summertime maximum and wintertime minimum in AC volume transport is robust across the 3-year period of *in-situ* observations from 2010-2013 [Beal et al., 2015], the 22 year proxy from 1993-2015 [Beal and Elipot, 2016], and for the 1999-2009 period coinciding with QuikSCAT measurements. This seasonal transport signal matches that observed in surface geostrophic currents [Krug and Tournadre, 2012], but is different from the seasonality previously reported by modelling studies [Biastoch et al., 1999; Matano et al., 2002].

Theory suggests that the variability of the AC will be related to the large-scale wind stress pattern over the Southern Indian Ocean (Figure 1). When there is an alteration in wind stress curl (WSC) over the Indian Ocean, there is an adjustment of the circulation within the basin, ultimately resulting in a modification in the volume transport of the western boundary current [Stommel, 1948; Gill, 1982]. This adjustment to WSC variability is not instantaneous, as it is communicated across the basin by Rossby waves with varying propagation speeds depending on the mode of the wave [Gill, 1982; Killworth, 2001; Subrahmanyam et al., 2001]. At the latitude of the ACT line (34.5°S) the seasonal cycle of the Sverdrup transport driven by winds across the basin is opposite to the seasonal cycle of AC transport (Figure 2).

Hence, we hypothesize that winds over the Southern Indian Ocean should play a critical role in determining the seasonal phasing of the AC and we use simple shallow water models to investigate the contributions of the barotropic and first baroclinic mode adjustments to local, near-field, and far-field wind forcing. This is not a theoretical study into wind driven ocean circulation as the theory has been well covered by the work of Anderson and Killworth [1977], Anderson and Corry [1985], and Kamenkovich and Pedlosky [1996] among others. Instead we hope to gain some insight into the dominant mechanisms setting the seasonal phasing of the western boundary current at the location of the ACT line. To do this we use QuikSCAT wind stress climatology to force single layer and $1\ \frac{1}{2}$ layer shallow water ocean models. Idealized models are chosen for the purposes of this study instead of using multi-layer more realistic models as the more simple approach to the problem enables the identification of the individual influences of the barotropic and first baroclinic mode adjustment processes as well as the sensitivity of the seasonal phasing to winds in different areas of the basin.

This study is the first to use a combination of *in-situ* observations, satellite measurements, and idealized ocean models to obtain a better understanding of the drivers of the observed seasonal phasing of the AC.

2 Data and Methods

2.1 Shallow Water Models

The Regional Ocean Modelling System (ROMS) is used as a platform from which to run idealized shallow water models. ROMS is a four dimensional free surface, terrain-following coordinates, realistic ocean model [Shchepetkin and McWilliams, 2005]. It solves the barotropic and baroclinic components of the primitive equations separately using a 'time-split' technique. Here we use the barotropic subsystem of ROMS to run simple, wind driven, shallow water models as done by LaCasce and Isachsen [2007]. The grid size is 1/3° (31.5 km), and the domain is limited to the Southern Indian Ocean (5°S - 50°S, 19°E - 119°E). The boundaries are closed and no-slip, with a turbulent Laplacian viscosity for velocity of 500 m^2/s, and the frictional parameter, r, is large (3×10^{-4} m/s) in order to maintain stability. The models are only forced with climatological winds - there are no thermohaline processes- and run for 50 years with the first 20 years discarded as spin-up time.

Both the barotropic and first baroclinic mode models simulate the response of a single active layer to climatological winds. In the case of the barotropic model, this single layer represents the full water column and its base is set by the depth of the topography of the Southern Indian Ocean. We use ETOPO2 bathymetry [ETOPO2, 2006], a two arc minute ocean-floor elevation data-set, averaged to a final resolution of 55.2 km to avoid the creation of spurious circulation features in areas of rapidly changing topography. In the case of the first baroclinic mode model, the single layer lies over a passive ($\frac{1}{2}$) layer, and the interface between the active and passive layers can be thought of as the pycnocline, as it is defined by a step function in density. The model is spun up from an initial pycnocline depth informed by observations, with the heaving of the interface, and hence changes in thickness of the upper active layer, driven by wind stress at the surface. A frictional coefficient, r, is applied to the interface between the active and passive layers. Gravity, $g = 9.8$ m/s^2, is replaced by reduced gravity (g') which is dependent on the density gradient between the two layers:

$$g' = \left(\frac{\rho_2 - \rho_1}{\rho_0}\right) g \tag{1}$$

where ρ_1 is the constant density of the upper layer, ρ_2 is the constant density of the lower layer, and ρ_0 is the mean density of the water column.

2.2 QuikSCAT winds

The wind stress climatology used to force our shallow water models is from the NASA Quick Scatterometer (QuikSCAT) which retrieved surface winds from backscatter over the oceans for 10 years, between July 1999 and November 2009. From these data, Risien and Chelton [2008] created a Scatterometer Climatology of Ocean Winds (SCOW) at a 1/4° resolution. A comparison of wind atlases (QuikSCAT, ERA-Interim, ERS and NCEP-NCAR) showed that broad-scale features of seasonal WSC are robust between products, but QuikSCAT is able to resolve smaller scale features close to the boundaries of the Southern Indian Ocean which could be important drivers of variability in the AC.

2.3 Agulhas Current Time-series Data

The ACT experiment produced the longest continuous set of *in-situ* measurements of the AC to date, providing 34 months of velocity and transport data [Beal et al., 2015]. The array, nominally at 34.5°S, followed the path of the TOPEX/Jason-1-2 satellite altimeter groundtrack (Figure 1) and consisted of 7 full-depth current meter moorings and 4 current pressure inverted echo sounders (CPIES) [Beal et al., 2015]. Beal and Elipot [2016] built a statistical model to relate the local volume transport at each mooring and between each CPIES pair with the satellite measured sea surface slope during each altimeter pass, producing a proxy for AC volume transport spanning the period 1993-2015. Beal et al. [2015] defined two transport estimates, a stream-wise Tjet and a fixed boundary layer integration Tbox, and found that both have the same phasing of the seasonal cycle. Tbox is defined as the net transport 90° to the ACT line, integrated from the coast out to the time-mean position of the zero velocity isotach [Beal et al., 2015]. In this study, we use Tbox for comparison with our model results because it can be cleanly 'joined' with the interior ocean and region of wind forcing in the case of estimating the Sverdrup transport (Figure 2).

3 Results and Discussion

3.1 Seasonality of Southern Indian Ocean Winds

A plot of the annual mean QuikSCAT WSC over the Southern Indian Ocean (Figure 3a) shows the generally positive curl over the center of the basin, set up by the strong westerly winds in the southern portion of the domain (south of 40°S). An Empirical Orthogonal Function (EOF) analysis was used to explore the spatial variability of seasonal changes in the QuikSCAT WSC fields. The first EOF (Figure 3b) captures 55 % of the variance of the seasonal WSC. The spatial pattern of the anomalies indicates that the majority of the WSC variability over the Southern Indian Ocean is associated with seasonal meridional shifts in the winds, as the subtropics exhibit opposite seasonal anomalies to the southern portion of the domain. In austral summertime (December to April, Figure 3d), the principal component (PC) is negative. This indicates a stronger negative WSC over the tropics, weaker positive WSC over the mid-latitudes (20°S to 35°S), and stronger negative WSC south of 36°S. This corresponds to the more southerly position of the trade winds and the westerlies during austral summer. The pattern inverts during winter, when wind belts shift northwards, thereby strengthening the positive WSC over the subtropics, and decreasing the strength of the negative WSC over the tropics.

Seasonal WSC changes at the mean latitude of the ACT line (34.5°S; dotted line Figures 3b) are not zonally coherent, and therefore a simple spin-up, spin-down and/or shifting of the gyre is not the whole picture. In summertime the WSC over the eastern and western boundaries has a strong positive anomaly while the anomalies over the center of the basin are small and negative (Figure 3c). In winter, the opposite is true, where the WSC at the eastern and western boundaries drops in strength, and the curl over the center of the basin increases.

3.2 Barotropic Model

We start by exploring the barotropic adjustment of the Southern Indian Ocean to the seasonal wind forcing (Figure 3). The mean circulation simulated by the barotropic model is strongly constrained by topography, such that in place of a single subtropical gyre, there are smaller sub-gyres delineated by f/H contours (Figures 4a and b). According to the Topographic Sverdrup Relation:

$$\vec{U}.\vec{\nabla}\left(\frac{f}{H}\right) = \vec{\nabla} \times \left(\frac{\tau}{H}\right) \tag{2}$$

for a homogenous layer of variable depth H, mass transport ($\vec{U} = H\vec{u}$) is driven across f/H contours by the curl of wind stress over water column depth ($\frac{\tau}{H}$). Hence where there is a weak curl, such as over the western Southern Indian Ocean (Figure 3a), the circulation will be parallel to f/H isolines, thereby creating subgyres (Figure 4a and b). Bathymetric barriers shallower than 2000 m such as the Southwest Indian Ocean Ridge, the Madagascar Plateau, and the Mozambique Ridge largely block the western boundary from a barotropic adjustment originating in the eastern portion of the basin. In this model, the main western boundary current does not penetrate onto the South African continental slope, but instead follows the Mozambique Ridge southwards (Figure 4a).

To compare the seasonality of the modelled AC to that observed by the ACT proxy, we calculate the boundary layer transport in the same way as done by Beal et al. [2015] and at the same location (Figure 4a). The volume transport is small, as the majority of the flow is deflected offshore, with the maximum south-westward transport occurring in November (Spring) and the minimum in May (Autumn) (Figure 4c). The seasonal phasing is similar to the seasonality reported by Biastoch et al. [1999] and Matano et al. [2002], even though the volume transport is far less. They argued that the AC's seasonality was advected from the Mozambique Channel with a delay of approximately two to three months, while signals directly from the east were blocked by topography. A similar connection is apparent in our model where the peak in southward flow through the Mozambique Channel at 23°S is in June (Figure 4d), 5 months ahead of the simulated AC seasonal cycle. Whilst the results from our barotropic simulation are similar to the two previous model studies of AC seasonality [Biastoch et al., 1999; Matano et al., 1999, 2002], they do not capture the observed seasonality of the AC and our findings suggest that the observed summertime maximum in AC flow must be set by other processes.

3.3 First Baroclinic Mode Model Initialized with Realistic Reduced Gravity Parameters

Moving beyond the simplest case of a barotropic model, we now investigate the first baroclinic mode adjustment to climatological wind forcing over the Southern Indian Ocean using a 1 $\frac{1}{2}$ layer reduced gravity model. The set-up of this model is similar to that of Meyers [1979] for the North Pacific, in that there is a single active layer, the depth of which is driven only by wind stress forcing. The baroclinic model is initialized to the same pycnocline depth and reduced gravity everywhere. To inform a realistic upper layer thickness, density profiles for the Southern Indian Ocean for the latitude range of the ACT line were obtained from the World Ocean Atlas [WOA, 2013]. The mean pycnocline depth was found to be 800 m, with a mean density of the upper layer of $\rho_1 = 1026.2\ kg/m^3$ and a mean density of the lower layer of $\rho_2 = 1027.6\ kg/m^3$, giving a reduced gravity parameter of $g' = 0.0134\ m/s$.

The model's mean circulation (Figure 5a) compares well with that observed at steric heights of 200 m and 400 m from mapped Argo profiles referenced to 2000 m [Ridgway, 2007; Roemmich and Gilson, 2009]. At the surface, the reduced gravity model differs from the observed surface circulation (Figure 1) because there is no Indonesian Throughflow (ITF) in the model. The buoyancy driven thermohaline overturning is not simulated by the model either, and the lack of a Southern Hemisphere supergyre means that the finer features of the Agulhas Retroflection and Agulhas Return Current are missing. Results from the Agulhas Undercurrent Experiment suggested that there was no inertial recirculation of the AC between 30°S and 36°S [Casal et al., 2009]. We thus assume that the absence of the Retroflection and Return Current in the model is not critical for the investigation into AC seasonality at 34.5°S.

The simulated flow at the location of the ACT array has a mean south-westward speed of 0.24 m/s, a maximum speed of 0.60 m/s, the average flow is 224 km wide and 946 m deep. The simulated AC is slower than observed by the ACT *in-situ* measurements, which exhibits a mean south-westward speed out to 224 km and over the upper 946 m of 0.39 m/s, and a maximum speed of 1.07 m/s. The Rossby radius of deformation in the model at the ACT line is 45 km, 10 km larger than estimated using observations in the AC area [Chelton et al., 1998].

The seasonality of the AC boundary layer transport from the model is at a maximum in November and at a minimum in June (Figure 5b). This seasonal phasing does not match that observed, with the maximum in flow occurring 4 months earlier in the simulation. Furthermore, the amplitude of seasonal changes is small at 4.5 Sv, 9.6% of the total transport, compared to the observed 22 Sv, 25% of the total transport (Figure 2). To understand more about what influences the amplitude and phasing of the simulated seasonal cycle, we experiment with the frictional dissipation and Rossby wave speeds in the model.

3.3.1 Role of friction in the model

For stability reasons, frictional dissipation (r) is large in the reduced gravity model. This frictional term represents the drag that the upper layer experiences as a result of its movement relative to the lower stationary layer. From a scaling analysis for a 1000 m layer and a velocity in the order of 0.1 m/s, the frictional parameter used in the simulations ($r = 3 \times 10^{-4}$ m/s) is equivalent to a vertical turbulent eddy viscosity of 0.3 m^2/s. This is three to four orders of magnitude larger than reality [Munk, 1966; Gregg, 1987; Ledwell et al., 1998] and may partially explain the unrealistically small amplitude in the seasonal cycle of the simulated AC (Figure 5b). Chassignet and Garraffo [2001] showed how the amplitude of their modelled circulation was highly sensitive to the choice of viscosity magnitude. To investigate the effect of this frictional coefficient on the simulated AC, the frictional parameter used in the initial run was reduced by an order of magnitude. Figure 5b shows the seasonal cycle of the simulated AC in the reduced gravity model with the original friction (solid line), compared to the seasonal cycle in the reduced friction case (dashed line). The seasonal phasing is not altered by a decrease in friction, but the amplitude doubles, from 4.5 Sv to 9.8 Sv, and the mean transport of the current increases by 3.9 Sv. Note that more noise is introduced into the model solution by reducing friction, as is evident by the larger width of the 95% confidence interval on the seasonal cycle in the reduced friction case. For both simulations, however, the standard error is small as there is no inter-annual variability in the forcing. This is the advantage of running idealized experiments - the focus is on the adjustment process without interference from variability and oceanic turbulence as can happen in more realistic multi-layer models.

For further experimentation it is necessary to keep the higher frictional coefficient to stabilize the simulations and prevent outcropping of the pycnocline at the eastern boundary. The original frictional parameter is maintained with the knowledge that a decrease in this value does not affect the seasonal phasing of the AC, but does increase the amplitude of the seasonal cycle.

3.3.2 First Baroclinic Mode Rossby Wave Speeds

To explore the role of Rossby waves in influencing AC seasonality, the propagation of anomalies across the Southern Indian Ocean at the latitude of the ACT line is investigated. We first calculate the observed Rossby wave propagation speed using a Radon Transform on Sea Level Anomaly (SLA) data [Cipollini et al., 2006] from AVISO (Archiving, Validation and Interpretation of Satellite Oceanographic data). The Radon Transform searches for the direction of largest signal intensity along a line in longitude-time space, and determines the speed of signal propagation [Cipollini et al., 2006; De La Rosa et al., 2007]. A limitation of the 2D transform is that the minimum speed detected is 1.5 km/day, as the angle associated with slow propagation speeds is too small for the transform to detect.

Results from a 2D Radon Transform show sizeable variation in propagation speed with longitude (Figure 6a). Along the latitude band of the ACT line, anomalies propagate slowly in the eastern portion of the basin, slow down even further to below 1.5 km/day at all latitudes over the longitude range 75°E to 95°E, and then speed up towards the western boundary (Figure 6a). This westward increase in Rossby wave propagation speed can be explained in part by an increase in the radius of deformation as pycnocline depth (along with sea surface height) increases westwards until just outside the western boundary current due to the geostrophic circulation of the gyre. This cannot, however, explain why there is a region of elevated propagation speeds around 100°E, and why speeds then drop in the center of the basin. This pattern does not relate to bathymetry across the basin. Birol and Morrow [2001] found that a wind-forced model was able to reproduce observed baroclinic Rossby wave variability around the 90° Ridge even though the model possessed no bathymetry, as the observed changes in baroclinic Rossby wave characteristics were driven by modifications in wind forcing and not bathymetry [Hermes and Reason, 2009]. We thus hypothesise that constructive and destructive interference with local Ekman pumping driven by the overlying WSC may explain the changes in Rossby wave speed (Figure 6).

There is no evidence that WSC variance over the eastern portion of the basin reaches the western boundary (Figure 6b). Coherent bands of SLA are only seen to propagate to the western boundary from around 40°E (Figure 6b). The average propagation speed of SLA across the whole basin at the latitude of the ACT line is 3.3 km/day, while the average propagation speed from 40°E to the western boundary is 3.5 km/day (Figure 6). It is likely that the opposing patterns of seasonal WSC contribute to this interference.

To approximate Rossby wave propagation speed in the reduced gravity model, a negative anomaly initiated at the eastern boundary was tracked across the basin by eye (Figure 5c). A Radon Transform was not stable, due to the apparent infinite speeds observed mid-basin. On average, it takes an anomaly 1800 days to cross the 8040 km of the basin, equating to a mean propagation speed of 4.5 km/day. This is approximately 1 km/day faster than that observed from AVISO. Similar to AVISO observations (Figure 6), signals initiated at the eastern boundary only propagate to about 90°E and then die out. A similar phenomenon was identified by Qiu et al. [1997] in the North Pacific at high latitudes where the relatively slow moving Rossby waves appeared to be confined close to the eastern boundary as they dissipated shortly thereafter on their journey west. From around 95°E to 65°E, the reduced gravity ocean appears to respond instantaneously to local WSC forcing (Figure 5c). The reduced gravity model, by construction, does not have topography, as the bottom layer is infinitely deep. The changes in propagation speed therefore cannot be explained by interaction with ocean ridges, and so the observed dissipation of Rossby waves during their journey west in this simulation forced only by seasonal winds, acts to strengthen our previous hypothesis that destructive interference with overlying Ekman pumping and suction takes place. The absence of a coherent transmission of SLA across the Southern Indian Ocean basin suggests that the anomalies arriving at the western boundary are predominantly from the near-field area.

West of 60°E, a coherent propagation of SLA into the western boundary can be seen with negative anomalies arriving just before the end of the year (Figure 5c), coinciding with the November peak of the AC seasonal cycle (Figure 5b). The sign of anomalies at the western boundary (27°E-30°E) are opposite to the sign of anomalies around 40°E for each season (Figure 5c). This is consistent with the change in seasonal WSC identified in the EOF analysis over this longitude range (Figure 3).

If we track an anomaly from 40°E to the western boundary, it takes half a year to get there, equating to a propagation speed of 6.2 km/day. This is almost double the average speed of an anomaly from 40°E to the western boundary observed in AVISO SLA data of 3.5 km/day (Figure 6a). The difference in the near-field propagation speeds equals approximately 4.6 months lag time, and may be the reason that the seasonal phasing in the model (Figure 5b) is different to that observed (Figure 2).

3.3.3 Sensitivity of Simulated Seasonal Cycle to Reduced Gravity Parameters

Next, we explore the affect of changing the magnitude of the reduced gravity parameters H_0 and g', which influence the basin-wide pycnocline slope, the Rossby wave deformation radius, and thus the propagation speed in the reduced gravity model. These parameters determine the adjustment time to winds through Rossby wave propagation speed by:

$$C_1 = -\beta \left(\frac{g' H}{f^2} \right) \tag{3}$$

where C_1 is the first baroclinic mode Rossby wave speed, β is the gradient of Earth's planetary vorticity, and f is the Coriolis parameter. We test the influence of the density difference ($\triangle\rho$) between the active and passive layers of the reduced gravity model (expressed in g', Equation 1), and the initial depth of the active layer (H_0), on the amplitude and phase of the AC seasonal cycle. To isolate the respective effects, one of the parameters is incrementally increased in value, while the other is kept fixed (Figure 7). Increasing the active layer/pycnocline depth (H_0) results in a shift of the seasonal phasing backwards in time, with a deeper pycnocline resulting in a greater mean transport and larger seasonal amplitude (Figure 7). An increase in the density gradient between the two layers (bigger g') also results in a larger seasonal amplitude, and a backwards shift in the seasonal phasing as predicted by Equation 3, although the response is not simply linear owing to the heterogeneity of WSC forcing and the integration and interference of Rossby wave signals. If either g' or H_0 are increased, WSC forcing signals will be communicated faster to the western boundary, resulting in a backwards shift in the seasonal phasing.

In Figure 7b, a sixth model simulation is included where the initial radius of deformation is set at 30 km and the seasonal cycle of the AC (magenta) is maximum in February and minimum in July, agreeing well with observations. It was not possible to initialize a simulation with a radius of deformation of 30 km and a pycnocline depth of less than 500 m as the pycnocline outcrops and the model blows up.

3.3.4 Correctly Simulating Adjustment Time to Wind Forcing

In our first reduced gravity simulation, the initial parameters were chosen so that H_0 equalled the mean depth of the pycnocline across the Southern Indian Ocean at the latitude of the ACT line (800 m), and the reduced gravity parameter ($g' = 0.0134\ m/s^2$) represented the observed density difference between the upper 800 m and the lower layer. These 'realistic' parameters, did not, however, correctly represent phase speeds of baroclinic waves observed in the Southern Indian Ocean, and thus the arrival time of the wind stress signal at the western boundary.

In our next simulation, the propagation speeds of anomalies in the model are in line with those observed in reality, both basin-wide and in the critical near-field area. For this experiment we forced the model with the same initial active layer depth, but a smaller reduced gravity, $g' = 0.0076\ m/s^2$ (Figure 8).

The mean radius of deformation at the ACT line is now 34 km (Figure 8a), matching the observations of Chelton et al. [1998]. In this simulation, the boundary flow (1051 m deep) is on average deeper than in the first simulation, and the mean flow is larger at -48.9 Sv. This compares well with the Sverdrup transport at the location of the ACT line of -49 Sv (Figure 2). The mean flow of the upper 1051 m at the ACT line from 2010-2013 when the ACT moorings were in place was -68 Sv. The difference of 19 Sv is similar to the combined volume transports of the buoyancy driven overturning circulation and the Indonesian Throughflow [Sprintall et al., 2009; Le Bars et al., 2013], both of which are absent in the model. The seasonal cycle of the current in this simulation is maximum in February-March and minimum in July-August (Figure 8b), agreeing well with the observed phasing (Figure 2), but with a smaller amplitude than observed.

The propagation of simulated anomalies across the Southern Indian Ocean at the mean latitude of the ACT line (Figure 8c) shows similar characteristics to the observations (Figure 6). An anomaly is initiated at the eastern boundary, propagates to about 100°E and then dies out. Thereafter, across the central region of the basin, the sea surface height (SSH) responds directly to overlying seasonal WSC changes with no incoming signals to alter the local SSH (see Figure 3b). Signals arriving at the western boundary appear to originate from the near field area- this will be explored further in the next section. Tracking by eye the propagation of a negative SLA across the basin (Figure 8c), reveals a mean phase speed of first baroclinic mode Rossby waves of approximately 3.2 km/day, which almost matches that calculated from AVISO observations (3.3 km/day; Figure 6). It takes approximately 1 year for an anomaly to reach the western boundary from 40°E, equating to a mean propagation speed in this area of 3.1 km/day. This is much closer to the observed AVISO SLA mean propagation speed west of 40°E (3.5 km/day) when compared to the propagation speeds of the first experiment (6.2 km/day; Figure 5c), which may explain why the seasonal phasing is more in line with observations.

When propagation speeds in the reduced gravity model are close to those observed in reality, lag time for the communication of near-field wind stress anomalies to the western boundary is more realistic, and consequently the simulated AC possesses a seasonal phasing that matches observations. However, while the mean transport of the simulated AC is close to that expected for the wind driven gyre, the amplitude of the seasonal cycle is much smaller than observed (Figure 8). The simulated amplitude of 1.8 Sv is an order of magnitude smaller than that observed (Figure 2). The reason for this small amplitude could be a combination of the influence of a large frictional parameter and a smaller g' than observed. The same seasonal phasing with a larger seasonal amplitude could be attained by decreasing friction, but the model becomes unstable.

3.4 Role of Near- vs Far-field winds

Our model experiments have focused on the dependence of the seasonal phasing of the AC on basin-wide parameters, since the model is initialised with only one value of H_0, and g'. However, the resultant patterns of Rossby wave propagation suggest that the influence of winds on the AC is not uniform basin-wide, with signal propagation altered or interrupted during the journey across the basin. To understand which characteristics of Indian Ocean wind forcing predominantly influence the seasonal phasing at the western boundary, we separately look at the roles of zonally averaged winds, local winds, near- and far-field winds and mean background winds. To carry out these experiments we use the reduced gravity model that correctly simulated the observed AC phasing (Figure 8).

Figure 3 revealed that different areas of the basin have differing WSC seasonal anomalies at the latitude of the ACT line. To explore the sensitivity of the simulated AC seasonality to this zonal WSC variability, the $1\,\frac{1}{2}$ layer reduced gravity model is forced with zonally averaged wind stresses for each month. The seasonal cycle of transport at the ACT line from this simulation (Figure 9a) is shifted backwards in time by 3 months compared to the simulation with real winds (Figure 8b), to give a December maximum in transport. However, the July minimum is preserved, suggesting that longitudinal variations in wind stress do not have a dominant influence on seasonality. Without the zonal variations in WSC, the instantaneous nature of the sea level response in the central region of the basin is clearer (Figure 9b). A negative WSC anomaly along the Australian coastline in summer, or a positive anomaly in winter, kicks off a disturbance at the eastern boundary of the basin which propagates coherently westwards to only 105°E over a period of 6 months. Thereafter, the magnitude of the SLA is decayed as it encounters destructive interferences with overlying WSC. The rest of the basin experiences an instantaneous adjustment to wind stress forcing as it receives no signals from incoming Rossby waves. Fu and Qiu [2002] also showed that the majority of the SSH variability over the interior of the ocean basin in the mid-latitudes is generated by the overlying WSC and not by incoming SSH anomalies. Seasonal changes at the western boundary therefore appear to be forced by winds only in the local area (Figure 9b).

Next, we investigate the influence of local winds that overlie the AC explicitly, by forcing with only seasonally varying winds directly over the AC, and annual mean winds over the rest of the basin. Local winds could drive seasonal upwelling and downwelling along the coast, which would in turn influence the pycnocline gradient and alter the AC volume transport. A hyporbolic tangent smoothing function was used over an area of 4° longitude from 29°E to 33°E to join the seasonal region with the mean interior. The seasonal phasing of the AC from this simulation (Figure 10a) is very similar to that of the zonally-averaged case (Figure 9a), indicating that in both simulations, the western boundary response was dominated by local overlying wind forcing. A weak seasonal signal in SLA emanates from the eastern boundary even in the absence of seasonal wind forcing (Figure 10). A likely explanation for this is a Kelvin wave that rapidly communicates the anomalies in SSH experienced at the western boundary clockwise around the closed boundaries of the model basin. Whilst the seasonal cycle from this simulation is similar to that from the zonal mean wind test, neither is in line with observations, suggesting that local winds overlying the ACT line cannot, alone, explain the seasonal phasing and that winds from further afield must therefore have an important contribution.

We next experiment with the region over which seasonal wind forcing is applied to determine the longitude beyond which seasonal variations in WSC have little effect. First the seasonality of winds to the west of 40°E is preserved while winds to the east are fixed to their annual mean (red line Figure 11a). Then the inverse was applied so that remote winds in the eastern portion of the basin varied seasonally, while regional winds in the west were fixed to the annual mean (green line Figure 11a). The original seasonal cycle from the run with normal winds is shown in blue in Figure 11. Both seasonally varying regional winds (to the west of 40°E), and seasonally changing remote winds (to the east of 40°E), contribute to the observed seasonal cycle. However, by moving the dividing line between near-field and far-field winds 5° westwards to 35°E we find that the 'near-field' winds dominate the total seasonality at the western boundary, with the contribution from the far-field seasonal changes shown to be very small (Figure 11b). Far-field winds act to decrease the amplitude of the strong February maximum driven by near-field winds in the model.

Finally the influence of the pattern of mean WSC on the seasonal cycle at the western boundary is diagnosed (green Figure 11c). The mean WSC sets up the gyre, and thus the shape of the pycnocline (Figure 8a) upon which the SLA anomalies of Rossby waves propagate. The seasonal maximum of the AC (green Figure 11c) is shifted 3 months behind that belonging to the simulation with normal full wind stress forcing (blue), thus exposing the influence that the background winds have on the AC seasonality via their establishment of the background gyre. In this simulation the anomalies propagate on what is effectively a flat pycnocline. This explains why the choice of reduced gravity parameters have a significant influence on the AC seasonality, even though near-field winds were shown (Figure 11b) to have dominant effect. Reproducing a realistic background gyre is therefore important when endeavouring to simulate the AC seasonal variability. We initially used the mean Rossby wave propagation speed as a tool to verify that the model was correctly simulating the mean basin-wide gyre response to WSC.

To clarify the role of background circulation in communicating near-field wind anomalies to the western boundary, the model is forced only with wind stress anomalies west of 35°E and zero wind forcing in the rest of the basin (red Figure 11c). The AC transport now possesses a peak in south-westward flow in March and the wintertime minimum is shifted slightly to earlier in the year. The phasing is similar to the seasonal cycle from normal wind forcing, but not identical, and the amplitude is almost half, highlighting the role of the shape of the background pycnocline in modulating the lag time needed for near-field wind signals to reach the western boundary.

4 Summary and Conclusions

The principal processes that contribute to the seasonality of the AC have, to date, remained largely unknown. In this study we explored the barotropic and baroclinic contributions to the seasonality of the AC, as well as the influence of local, near-field, and far-field winds. A single layer model was used to show that the barotropic contribution to the seasonality is small, as most of the signal is steered away from the South African continental shelf by the Mozambique Ridge.

A 1 $\frac{1}{2}$ layer reduced gravity model is able to capture the main features of the pycnocline circulation of the South Indian Ocean subtropical gyre. The seasonal cycle of the simulated AC was found to be highly sensitive to the initial conditions of reduced gravity and pycnocline depth as these parameters set the phase speed of propagating wind-driven disturbances in the system. When the active layer (H_0) is deepened, or the density gradient between the two layers (g') is increased, the adjustment time to WSC is shorter, and the seasonal cycle phasing shifts backwards in time.

A limitation of the reduced gravity model is that it cannot reproduce the observed amplitude of seasonal AC volume transport changes. While a larger seasonal variation in transport can be achieved by increasing g' or H_0, these parameters also influence the propagation speed of Rossby waves and result in a shift in the seasonal phasing of the simulated AC. Lowering friction increases the amplitude of the seasonal cycle, but renders the model unstable. It is, therefore, not possible to reproduce a seasonal cycle of the AC where both the amplitude and phasing match observations using a reduced gravity model. A model with Rossby wave propagation speeds in line with AVISO measurements, results in a seasonal cycle of AC transport similar to that observed, with a maximum in February-March and minimum in July-August.

Figure 12 shows the seasonal cycle of the AC from two recent ocean models of the AC: the Western Indian Ocean Energy Sink model (WOES; used for example by Ramanantsoa et al. [2018]), and a HYbrid Coordinate Ocean Model (HYCOM; Backeberg et al. [2014]). WOES is a ROMS/CROCO regional simulation with 60 vertical levels and three nested grids with resolution increasing from 1/4°, 1/12° to 1/36° over the AC. The HYCOM data is from a free-running HYCOM experiment used to generate the static ensemble in a data assimilation experiment of the Agulhas region at a 1/10° resolution with 30 vertical layers [Backeberg et al., 2014]. These simulations capture the wintertime minimum in flow, but the AC seasonal cycle is swamped by high sub-seasonal variance resulting in multiple peaks in flow (Figure 12). To the best of the authors' knowledge, there is no data published from realistic ocean models where the seasonal cycle of the AC matches that observed. This highlights a gap in the current capacity to simulate western boundary current seasonal variability and future work is planned by the authors where modern global ocean circulation models will be used to explore AC seasonality in different configurations.

The observed propagation of SLAs across the Southern Indian Ocean at the latitude of the ACT line suggested that signals from more remote wind forcing do not reach the western boundary and, indeed, our simulations corroborated this, showing that the influence of far-field winds on the seasonality of the AC is minor. Local winds over the ACT array are found to contribute a large part to the seasonality but cannot, alone, explain the observed seasonal phasing . Instead near-field winds to the west of 35°E are found to reproduce the observed AC phasing, thereby revealing the decisive contribution of the first order baroclinic mode adjustment to near-field winds in determining the seasonal phasing of the AC.

The importance of the background circulation set up by mean WSC was elucidated when the model was forced with WSC anomalies only, and the seasonality of the AC shifted backwards by 3 months. The mean wind stress sets the scene regarding pycnocline depth, which in turn influences the phase speed of signals carrying the wind stress information. In summary, the seasonal variation of near-field winds is important in exciting SLA which propagate to the western boundary, while the mean winds over the whole basin set the shape of the gyre upon which the SLA are projected. Together, these two processes force a simulated AC with a seasonal cycle that exhibits a prolonged January-February-March maximum and July minimum, agreeing well with observations.

The sensitivity of the seasonal cycle to Rossby wave propagation speeds raises questions regarding how the seasonal phasing of the AC may be affected by modifications in ocean stratification due to climate change. Fyfe and Saenko [2007] looked at how the dynamics of Rossby waves may change in response to upper-ocean warming and the consequent alteration in density structure. Using climate model simulations of the North Pacific they found that anthropogenic warming of the upper ocean resulted in a speed up of baroclinic Rossby waves. Hypothetically, the same could apply for the Southern Indian Ocean where surface warming would act to increase the density gradient between the surface and deep ocean, and lead to a speed up of baroclinic Rossby waves. This could imply a backwards shift of the seasonal phasing of the AC. The response of western boundary current seasonality to climate change is an interesting avenue suggested for future research.

5 Acknowledgements

The authors would like to acknowledge the financial support necessary to carry out this research provided by the South African National Research Fund (DST-NRF PDP Professional Development Grant number 88741) and the South African Environmental Observations Network (SAEON). The authors would furthermore like to thank the following sources for the mobility grants provided: the South African National Antarctic Programme (SANAP; grant number: 466311), the French Institut de recherche pour le developpement (IRD with travel support provided through ICEMASA; grant number 426213 CMS 1039), the South African National Research fund KIC award (grant number 111529) and the US National Science Foundation (US NSF award number 1459543). The modelling tools ROMS-AGRIF and ROMS-TOOLS used here were provided by IRD. The data from the idealized model simulations are available online at the Zenodo repository with DOI: 10.5281/zenodo.1211515. The altimeter products distributed by AVISO were produced by Ssalto/Duacs, with support from Cnes (http://www. aviso.altimetry.fr/duacs/). The *in-situ* mooring data from the ACT experiment are archived with the NOAA National Centers for Environmental Information (https://www.ncei.noaa.gov), with access numbers 0156669 and 0156605.

References

Anderson, D. L. T. and R. A. Corry
1985. Ocean response to low frequency wind forcing with application to the seasonal variation in the Florida Straits-Gulf Stream transport. *Progress in Oceanography*, 14(1977):7–40.

Anderson, D. L. T. and P. D. Killworth
1977. Spin-up of a stratified ocean, with topography. *Deep-Sea Research*, 24(8):709–732.

Backeberg, B., F. Counillon, J. Johannessen, and M.-I. Pujol
2014. Assimilating along-track SLA data using the EnOI in an eddy resolving model of the Agulhas system. *Ocean Dynamics*, 64(8):1121–1136.

Beal, L. M., W. P. M. De Ruijter, A. Biastoch, and R. Zahn
2011. On the role of the Agulhas system in ocean circulation and climate. *Nature*, 472(7344):429–436.

Beal, L. M. and S. Elipot
2016. Broadening not strengthening of the Agulhas Current since the early 1990s. *Nature*, 540(7634):570.

Beal, L. M., S. Elipot, A. Houk, and G. M. Leber
2015. Capturing the Transport Variability of a Western Boundary Jet Results from the Agulhas Current Timeseries Experiment (ACT). *Journal of Physical Oceanography*, 45(5):1302–1324.

Biastoch, A., C. J. C. Reason, J. R. E. Lutjeharms, and O. Boebel
1999. The importance of flow in the Mozambique Channel to seasonality in the greater Agulhas Current system. *Geophysical Research Letters*, 26(21):3321–3324.

Birol, F. and R. Morrow
2001. Source of the baroclinic waves in the southeast Indian Ocean. *Journal of Geophysical Research: Oceans*, 106(C5):9145–9160.

Bryden, H. L., L. M. Beal, and L. M. Duncan
2005. Structure and transport of the Agulhas Current and its temporal variability. *Journal of Oceanography*, 61(3):479–492.

Casal, T. G. D., L. M. Beal, R. Lumpkin, and W. E. Johns
2009. Structure and downstream evolution of the Agulhas Current system during a quasi synoptic survey in February to March 2003. *Journal of Geophysical Research: Oceans*, 114(C3).

Chassignet, E. P. and Z. D. Garraffo
2001. Viscosity parameterization and the Gulf Stream separation. *From Stirring to Mixing in a Stratified Ocean. Proceedings Hawaiian Winter Workshop. Held in the University of Hawaii.*

Chelton, D. B., R. A. DeSzoeke, M. G. Schlax, K. El Naggar, and N. Siwertz
1998. Geographical Variability of the First Baroclinic Rossby Radius of Deformation. *J Phys Oceanogr*, 28(3):433–460.

Cipollini, P., G. D. Quartly, P. G. Challenor, D. Cromwell, and I. S. Robinson
2006. Remote sensing of extra-equatorial planetary waves. In *Manual of Remote Sensing*, volume 6, Pp. 61–84. American Society for Photogrammetry and Remote Sensing.

De La Rosa, S., P. Cipollini, and H. M. Snaith
2007. An application of the Radon transform to study planetary waves in the Indian Ocean. In *ESA Envisat Symposium (SP-636,), Montreux.*

Elipot, S. and L. M. Beal
2015. Characteristics, Energetics, and Origins of Agulhas Current Meanders and Their Limited Influence on Ring Shedding. *Journal of Physical Oceanography*, 45(9):2294–2314.

ETOPO2
2006. 2-minute Gridded Global Relief Data (ETOPO version 2). *National Oceanic and Atmospheric Administration National Geophysical Data Center.*

Fu, L.-L. and B. Qiu
2002. Low-frequency variability of the North Pacific Ocean: The roles of boundary- and wind-driven baroclinic Rossby waves. *Journal of Geophysical Research: Oceans*, 107(C12):3220.

Fyfe, J. C. and O. A. Saenko
2007. Anthropogenic speed up of oceanic planetary waves. *Geophysical Research Letters*, 34(10):12–15.

Gill, A.
1982. *Atmosphere-Ocean dynamics*, volume 30. Academic press.

Gregg, M. C.
1987. Diapycnal mixing in the thermocline: A review. *Journal of Geophysical Research: Oceans*, 92(C5):5249–5286.

Hermes, J. C. and C. J. C. Reason
2009. The sensitivity of the seychelles-chagos thermocline ridge to large-scale wind anomalies. *ICES Journal of Marine Science*, 66(7):1455–1466.

Kamenkovich, I. and J. Pedlosky
1996. Radiating instability of nonzonal ocean currents. *Journal of Physical Oceanography*, 2(26):622–643.

Killworth, P. D.
2001. Rossby waves. *Encyclopedia of Ocean Sciences, Academic Press , San Diego, USA.*, Pp. 2434–2443.

Krug, M. and J. Tournadre
2012. Satellite observations of an annual cycle in the Agulhas Current. *Geophysical Research Letters*, 39(15).

LaCasce, J. and P. Isachsen
2007. On Sverdrup Discontinuities and Vortices in the Southwest Indian Ocean. *Jounral of Physical Oceanography*, 37:2940–2950.

Le Bars, D. L. B., H. A. Dijkstra, and W. P. M. De Ruijter
2013. Impact of the Indonesian Throughflow on Agulhas leakage. *Ocean Science*, 10(5):773–785.

Leber, G. M. and L. M. Beal
2104. Evidence that Agulhas Current transport is maintained during a meander. *Geophysical Research: Oceans*, (119):3806–3817.

Ledwell, J. R., A. J. Watson, and C. S. Law
1998. Mixing of a tracer in the pycnocline. *Journal of Geophysical Research: Oceans*, 103(C10):21499–21529.

Matano, R. P., E. J. Beier, P. T. Strub, and R. Tokmakian
2002. Large scale forcing of the Agulhas variability: The seasonal cycle. *Journal of Physical Oceanography*, 32(4):1228–1241.

Matano, R. P., C. G. Simionato, and P. T. Strub
1999. Modeling the Wind-Driven Variability of the South Indian Ocean. *Journal of Physical Oceanography*, 29(2):217–230.

Meyers, G.
1979. On the annual Rossby wave in the tropical North Pacific Ocean. *Journal of Physical Oceanography*, 9:663–674.

Munk, W. H.
1966. Abyssal recipes. *Deep Sea Research*, 13(4):707–730.

Nauw, J., H. Van Aken, A. Webb, J. Lutjeharms, and W. De Ruijter
2008. Observations of the southern East Madagascar Current and undercurrent and countercurrent system. *Journal of Geophysical Research: Oceans*, 113.

Njouodo, A. S. N., S. Koseki, N. Keenlyside, and M. Rouault
2018. Atmospheric signature of the Agulhas Current. *Geophysical Research Letters*, 45.

Penven, P., J. R. E. Lutjeharms, and P. Florenchie
2006. Madagascar: A pacemaker for the Agulhas Current system? *Geophysical Research Letters*, 33(17).

Ponsoni, L., B. Aguiar-González, H. Ridderinkhof, and L. Maas
2016. The East Madagascar Current: Volume transport and variability based on long-term observations. *Journal of Physical Oceanography*, 46(4):1045–1065.

Qiu, B., W. Miao, and P. Muller
1997. Propagation and Decay of Forced and Free Baroclinic Rossby Waves in Off Equatorial Oceans. *Journal of Physical Oceanography*, 27(11):2405–2417.

Ramanantsoa, J. H., P. P., M. Krug, J. Gula, and M. Rouault
2018. Uncovering a new current: the South-west MAdagascar Coastal Current (SMACC). *Geophysical Research Letters*, 45.

Ridgway, K. R.
2007. Long-term trend and decadal variability of the southward penetration of the East Australian Current. *Geophysical Research Letters*, 34(13).
Risien, C. M. and D. B. Chelton
2008. A global climatology of surface wind and wind stress fields from eight years of QuikSCAT scatterometer data. *Journal of Physical Oceanography*, 38(11):2379–2413.
Roemmich, D. and J. Gilson
2009. The 2004-2008 mean and annual cycle of temperature, salinity, and steric height in the global ocean from the Argo Program. *Progress in Oceanography*, 82(2):81–100.
Schouten, M. W., W. P. M. Ruijter, P. J. Leeuwen, and J. R. E. Lutjeharms
2000. Translation, decay and splitting of Agulhas rings in the southeastern Atlantic Ocean. *Journal of Geophysical Research: Oceans*, 105(C9):21913–21925.
Shchepetkin, A. F. and J. C. McWilliams
2005. The regional oceanic modeling system (ROMS): a split-explicit, free-surface, topography-following-coordinate oceanic model. *Ocean Modelling*, 9(4):347–404.
Sprintall, J., S. E. Wijffels, R. Molcard, and I. Jaya
2009. Direct estimates of the Indonesian Throughflow entering the Indian Ocean: 2004-2006. *Journal of Geophysical Research: Oceans*, 114(C7).
Stommel, H.
1948. The westward intensification of wind-driven ocean currents. *Eos, Transactions American Geophysical Union*, 29(2):202–206.
Subrahmanyam, B., I. S. Robinson, J. R. Blundell, and P. G. Challenor
2001. Indian Ocean Rossby waves observed in TOPEX/POSEIDON altimeter data and in model simulations. *International Journal of Remote Sensing*, 22(1):141–167.
WOA
2013. World Ocean Atlas. *U.S. National Oceanic and Atmospheric Administration, National Oceanographic Data Center (NODC)*, V2.

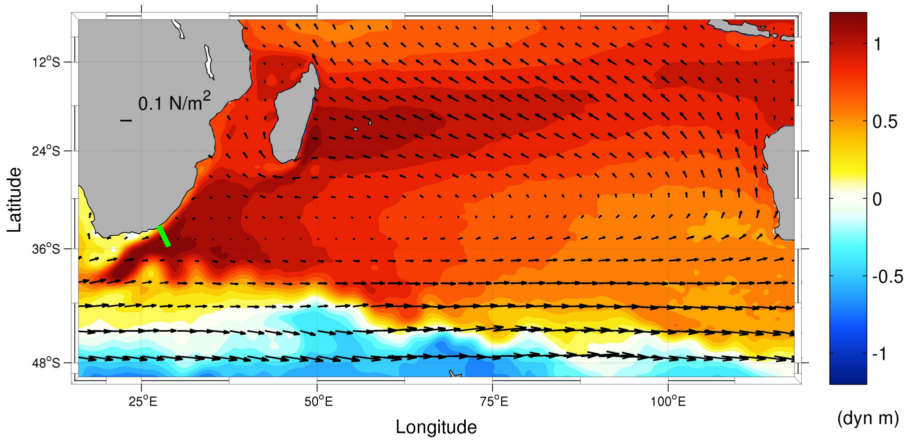

Figure 1. *Map showing mean AVISO sea surface height (SSH; dyn meters) of the Southern Indian Ocean with mean QuikSCAT wind stress overlaid. Wind stress vectors (N/m^2) are only shown for every 3.5° for clarity. Position of Agulhas Current Time-series (ACT) array is shown off the east coast of South Africa in green.*

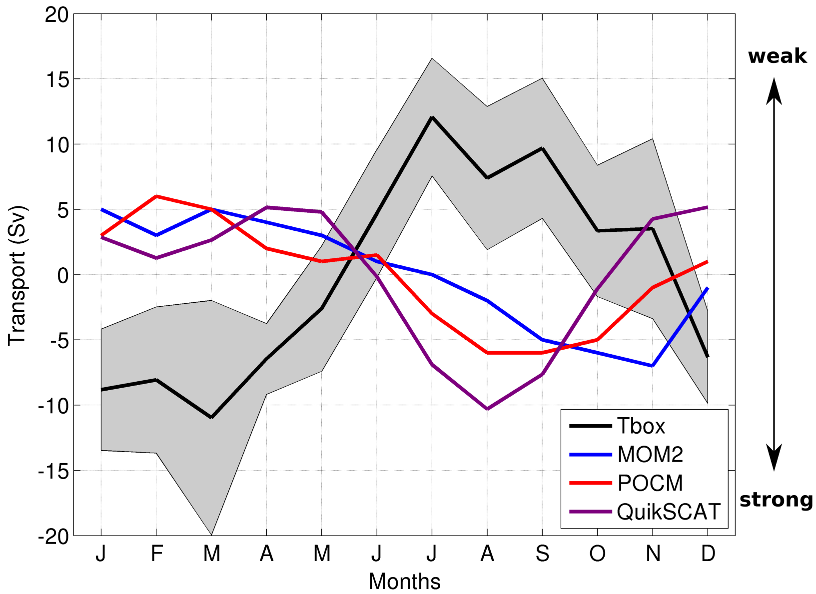

Figure 2. *Observed seasonal anomalies of the boundary layer transport (Tbox; black) from the ACT proxy time-series of Beal and Elipot [2016]. Solid black line shows the monthly mean values and shading shows the 95% confidence intervals. Shown for direct comparison are the seasonal anomalies in AC transport from the only two other publications on this topic: the Modular Oceans Model (MOM2; blue) of Biastoch et al. [1999], and the Parallel Ocean Circulation Model (POCM; red) of Matano et al. [2002]. Negative anomalies in transport indicate a stronger current as the AC flows south-westward. Also presented is the implied Sverdrup driven transport at the mean latitude of the ACT line (34.5° S) from QuikSCAT wind stress curl (purple).*

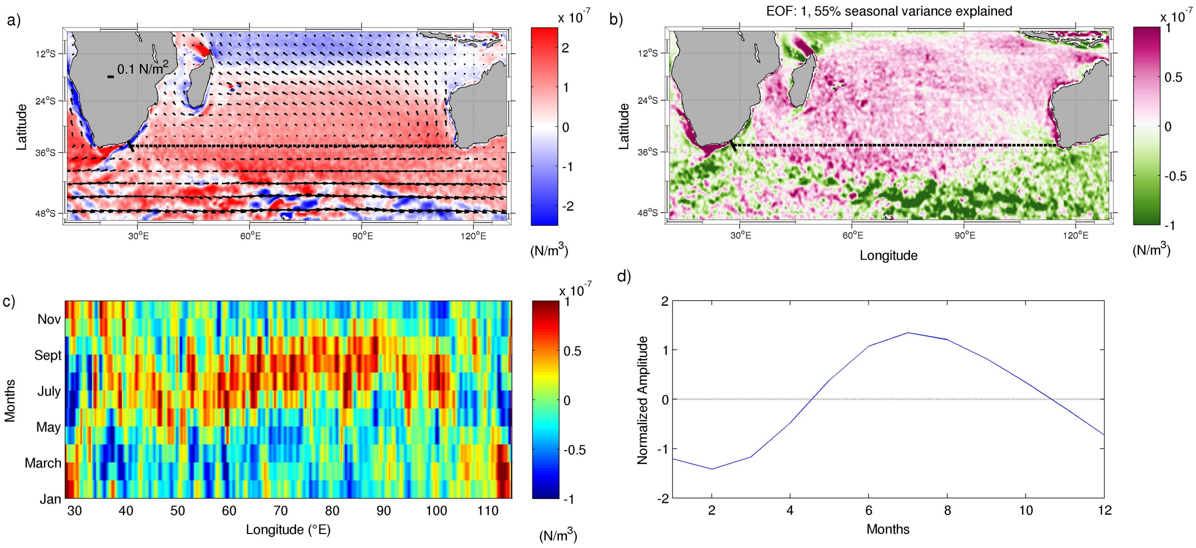

Figure 3. *Summary of seasonal QuikSCAT wind stress curl (WSC) alterations over the Southern Indian Ocean. a) Mean QuikSCAT WSC. b) First Empirical Orthogonal Function (EOF) of the climatological WSC. c) Hovmöller diagram showing the WSC anomalies across the Southern Indian Ocean at 34.5°S. d) The Principal Component (PC) of the first Empirical Orthogonal Function (EOF) shown in (b).*

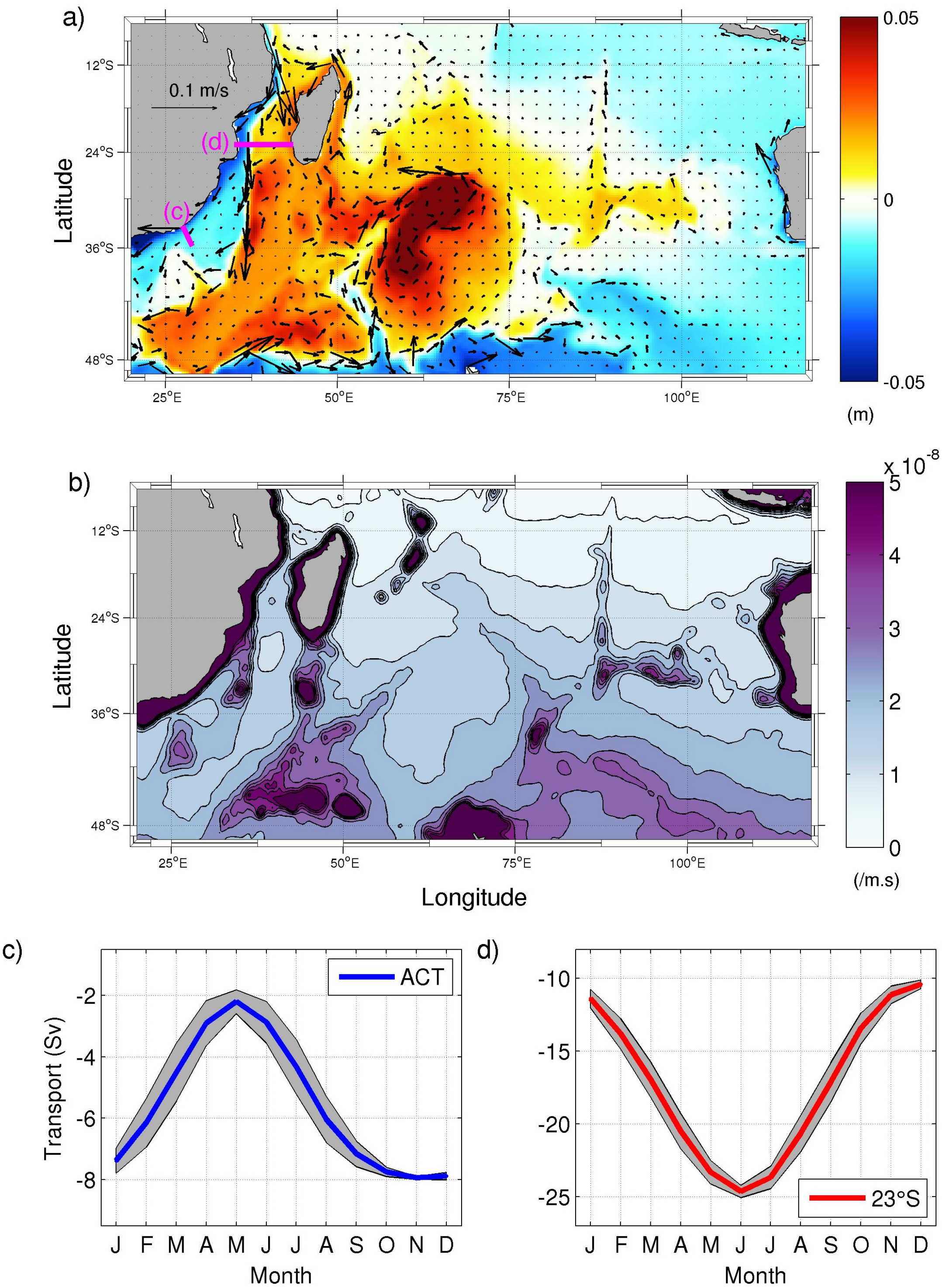

Figure 4. *a) Time mean sea surface height (m) of the barotropic model as background shading with vectors of mean circulation (m/s) overlaid. Location of sections corresponding to plots (c) and (d), are shown in magenta. b) Map of f/H contours for the Southern Indian Ocean. Seasonal cycle of volume transport at (c) the location of the Agulhas Current Time-series array, and (d) the Mozambique Channel at 23°S. Grey shading shows the 95% confidence interval of the seasonal cycle estimates.*

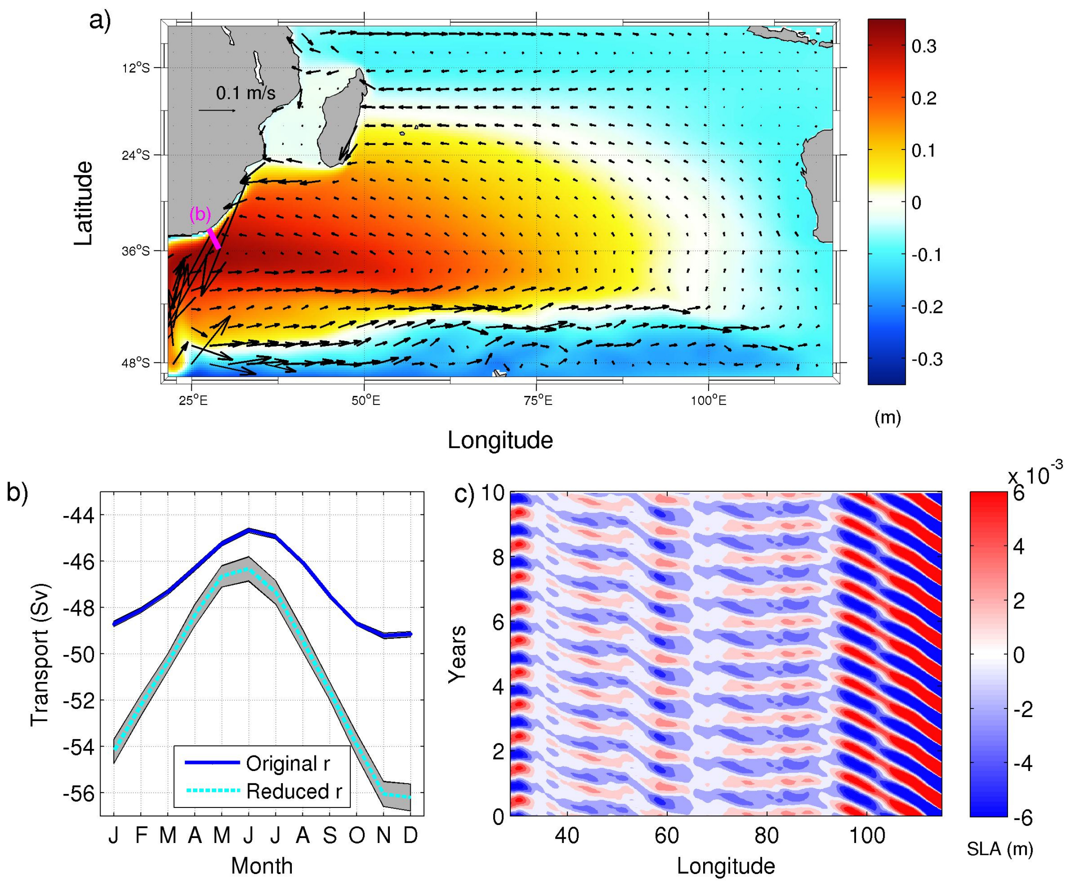

Figure 5. *a) Time mean sea surface height (m) of 1 $\frac{1}{2}$ layer reduced gravity model as background shading with vectors of mean circulation (m/s) overlaid. The position of the Agulhas Current Time-series array (ACT) is shown in magenta. b) Seasonal cycle of Agulhas Current transport (Sv) in simulation initiated with a thermocline depth of 800 m and $g' = 0.0134\ m/s^2$. Solid line shows seasonal cycle with the original frictional parameter of $3 \times 10^{-4}\ m/s$ and dashed line shows effect of reducing friction by an order of magnitude to $3 \times 10^{-5}\ m/s$. Grey shading shows 95% confidence interval on monthly means. c) Hovmöller plot showing the propagation of sea level anomalies (m) across the basin at the mean latitude of the ACT line (34.5°S) during the final 10 years of the simulation.*

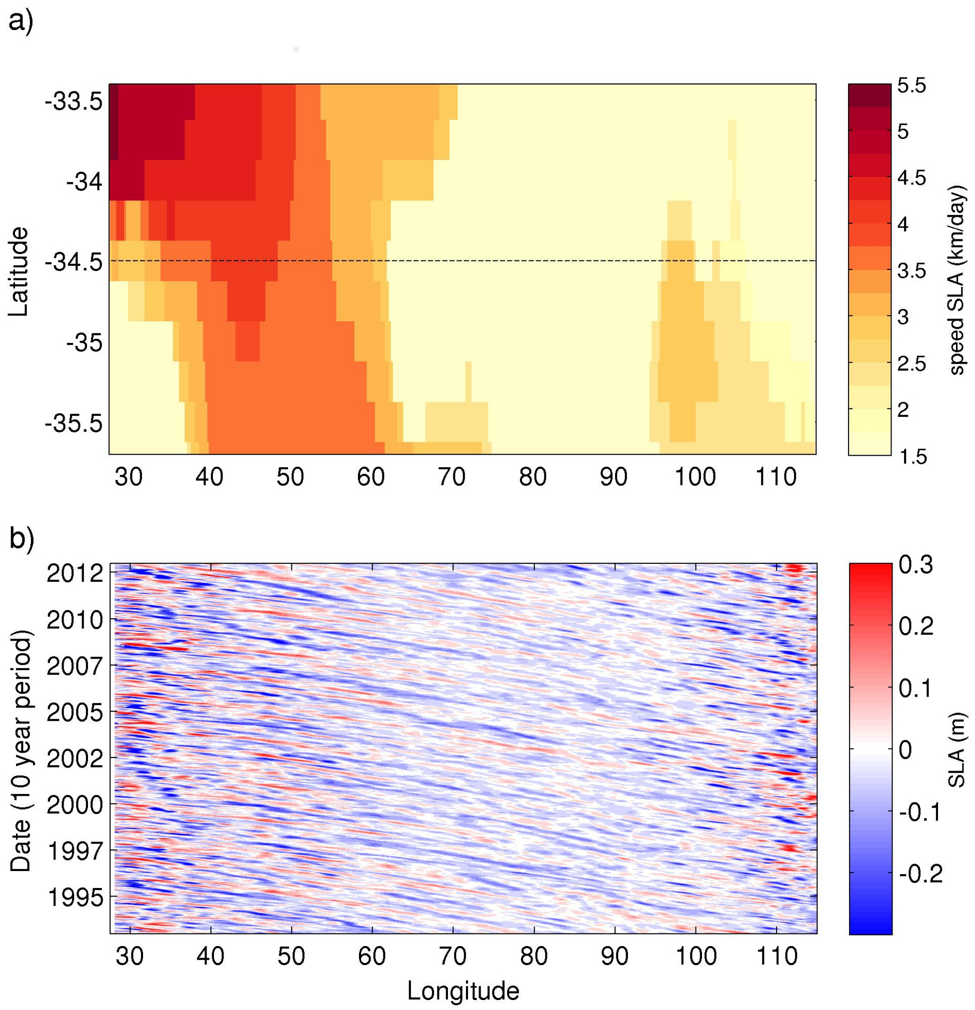

356 **Figure 6.** *a) Westward propagation speed (km/day) of Sea Level Anomalies (SLA) across the*
357 *Southern Indian Ocean from a 2D Radon Transform over the latitude range of the ACT line. b)*
358 *Hovmöller plot of SLA (m) at the mean latitude of the ACT line (34.5°S; dotted line in (a)).*

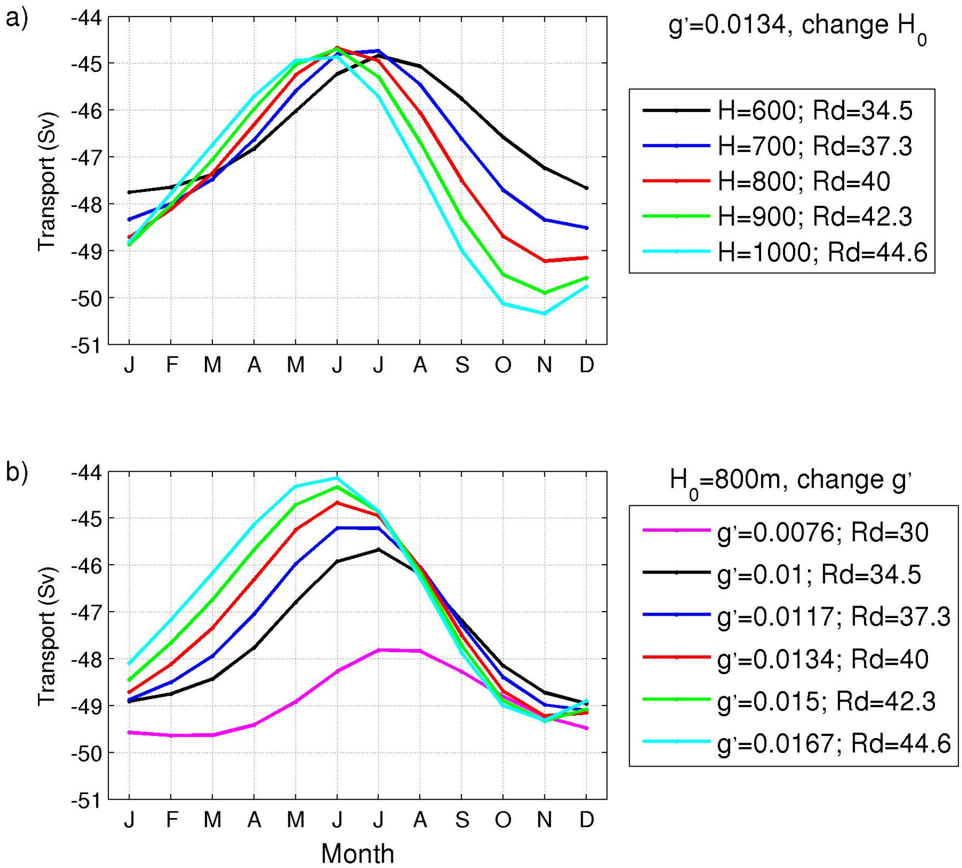

Figure 7. *Simulated seasonal cycle in volume transport (Sv) at the Agulhas Current Time-series array where (a) g' is set at 0.0134 m/s^2 and H_o is increased by 100 m increments, and (b) H_0 is set at 800 m and g' is increased so that the alterations in radius of deformation match those shown in plot (a). The resultant alterations in Rossby radius of deformation (Rd) are shown in the legend. An extra simulation is presented in (b) showing the effects of a further decrease in g' (magenta line).*

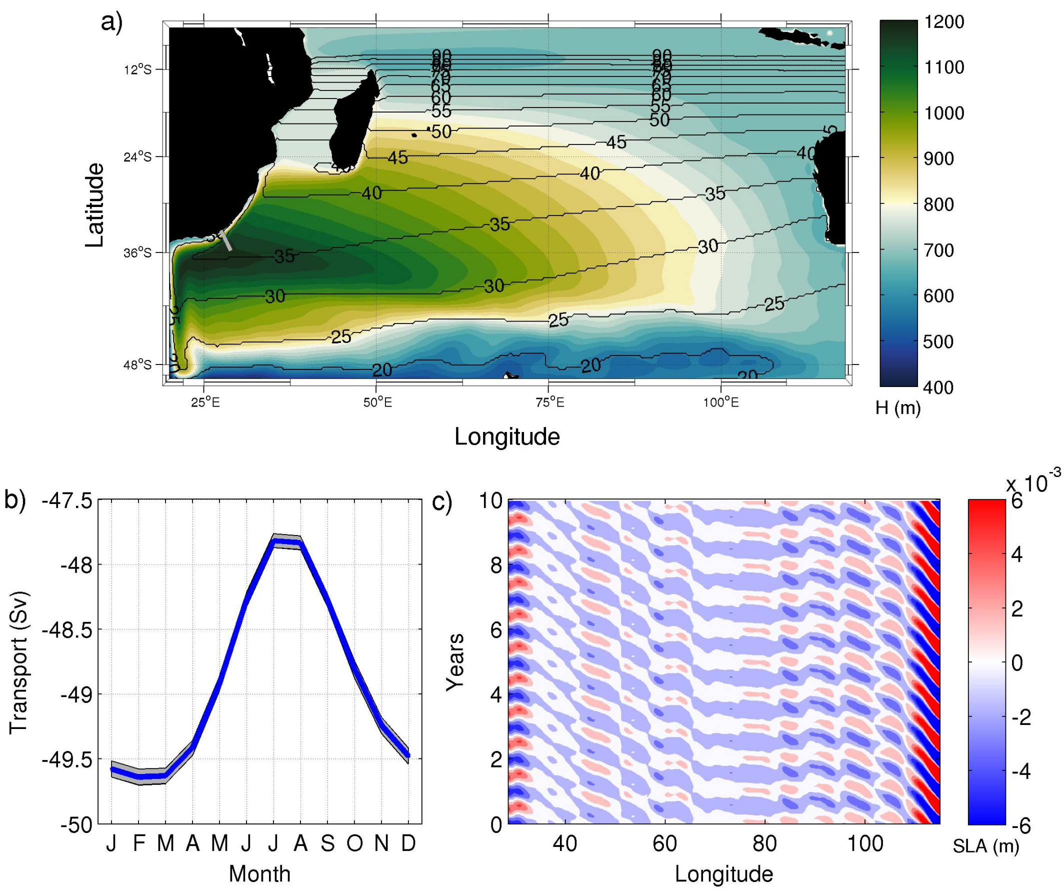

Figure 8. *a) Average depth of wind driven layer (m) as background shading with contours showing the corresponding Rossby radius of deformation (km) overlaid. The position of the Agulhas Current Time-series (ACT) array is shown in grey. b) Seasonal cycle of Agulhas Current transport (Sv) in the simulation initiated with a thermocline depth of 800 m and* $g' = 0.0076$ m/s^2*. Grey shading shows the 95% confidence interval of the seasonal cycle. c) Hovmöller plot showing the propagation of sea level anomalies (m) across the basin at the mean latitude of the ACT line (34.5° S) during the final 10 years of simulation.*

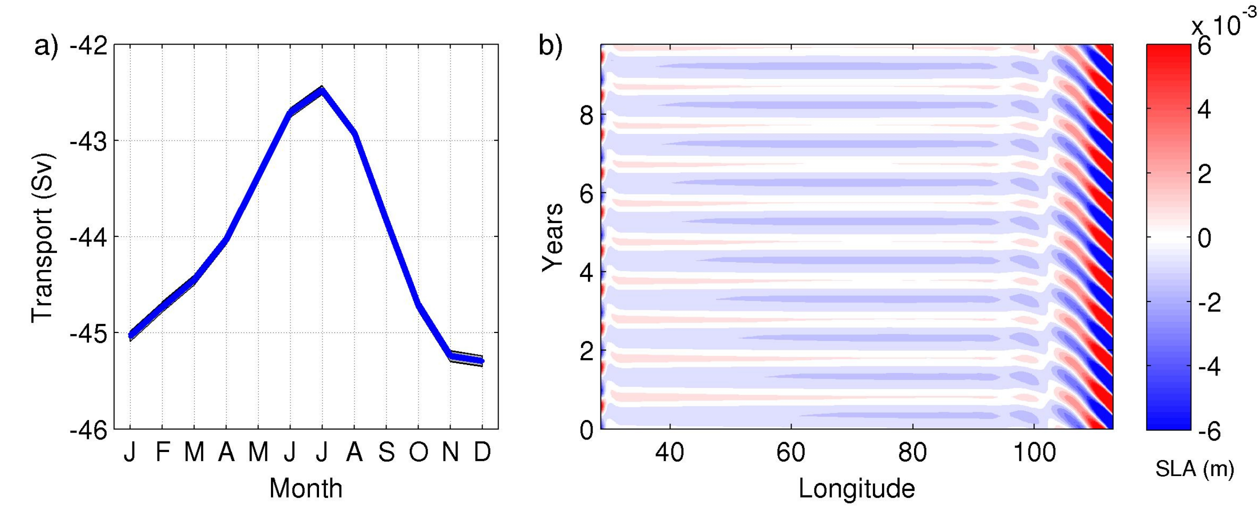

Figure 9. *a) Seasonal cycle for transport (Sv) across the Agulhas Current Time-series (ACT) line from a simulation forced by zonal mean wind stress curl. b) Hovmöller plot of sea level anomalies (SLA; m) at 34.5°S from reduced gravity model forced by only zonal mean winds.*

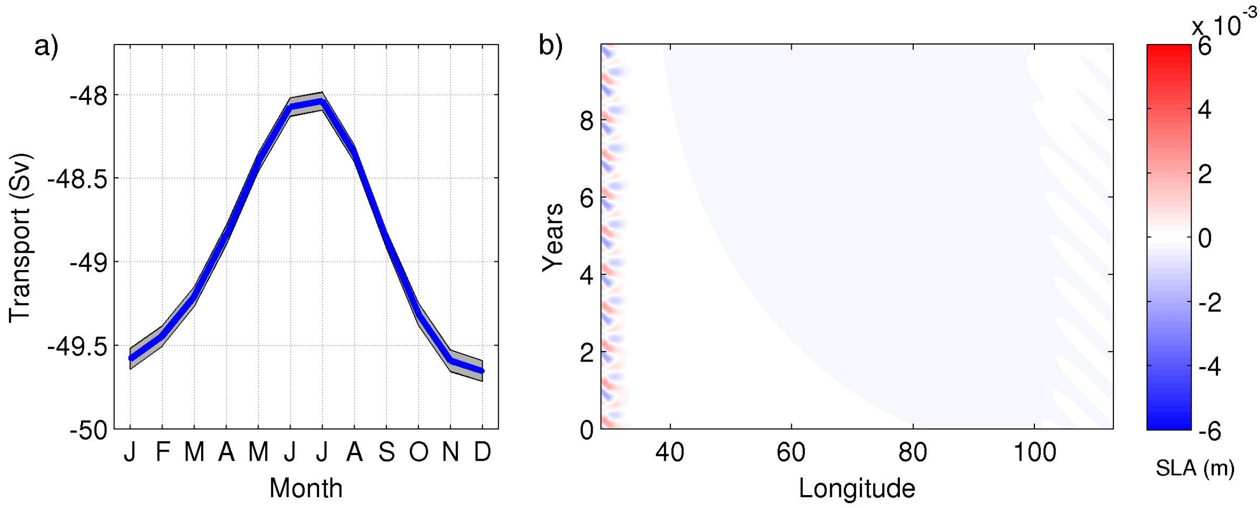

Figure 10. *a) Seasonal cycle for transport (Sv) across the Agulhas Current Time-series (ACT) line from reduced gravity model forced with seasonally varying winds to the west of 29°E, tapering off to no seasonality east of 33°E. b) Hovmöller plot of sea level anomalies (SLA; m) at 34.5°S.*

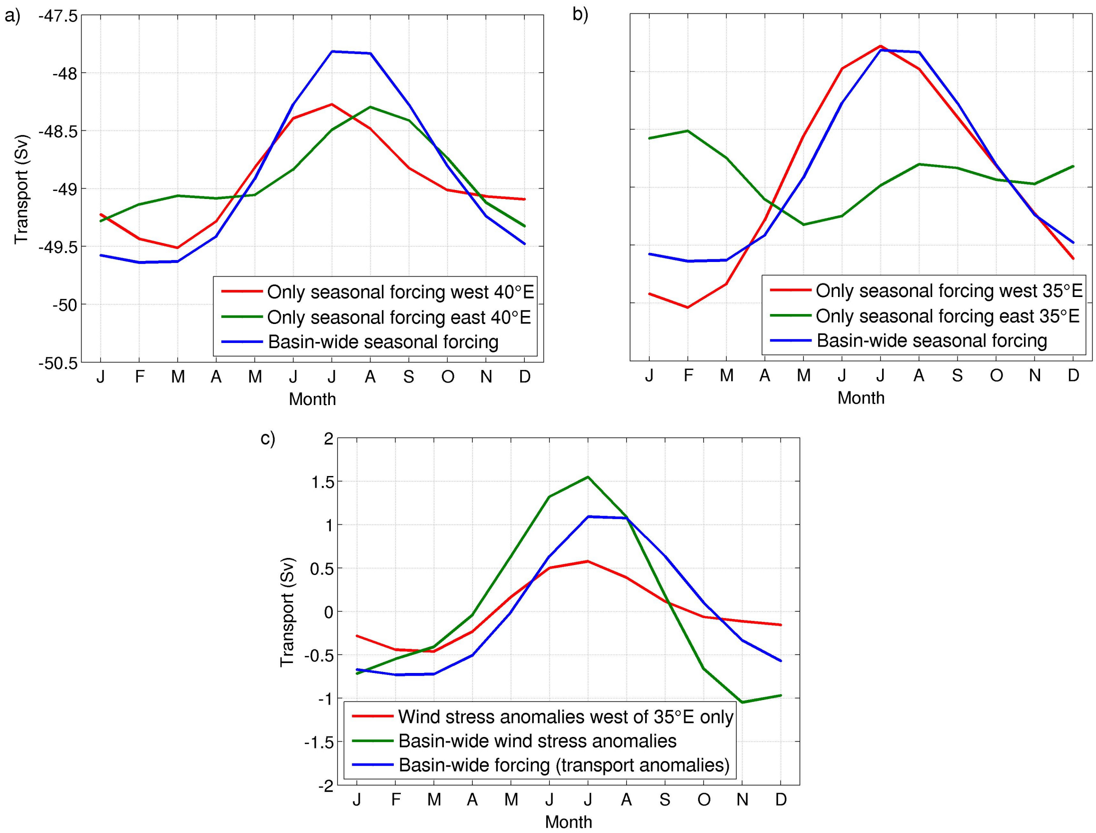

Figure 11. *Seasonal anomalies in transport (Sv) perpendicular to the Agulhas Current Time-series (ACT) line in simulations forced with seasonally varying winds in different portions of the basin. a) Regional (red) versus remote (green) seasonally varying wind stress. b) Near-field (red) versus far-field (green) seasonally varying wind stress. c) Simulation forced with only near field wind stress anomalies (red) and basin-wide wind stress anomalies only (green). In all plots the seasonal cycle of the AC in the model forced with basin-wide full seasonally varying wind stress is shown in blue, in plot (c) the transport anomalies are shown so that amplitude comparisons can be made with the transports from the simulations forced with only wind stress anomalies.*

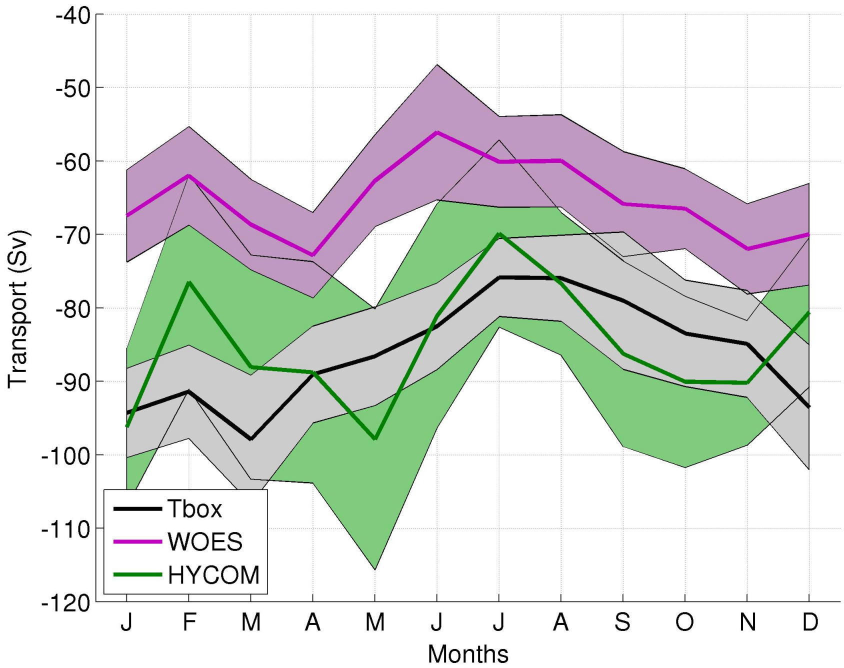

613 **Figure 12.** *Comparison of seasonal cycles in AC transport with 95% confidence shading. ACT*
614 *boundary layer transport from proxy time-series (1993-2015) shown in black, Western Indian*
615 *Ocean Sink model (WOES, 1993-2015, Ramanantsoa et al. [2018]) shown in purple, and HYbrid*
616 *Coordinate Ocean Model (HYCOM, 1993-2015, Backeberg et al. [2014]) shown in green*